PHYSICAL REVIEW B **96**, 014437 (2017)

Magnetic properties of the CrMnFeCoNi high-entropy alloy

Oldřich Schneeweiss,[1] Martin Friák,[1,2] Marie Dudová,[1] David Holec,[3] Mojmír Šob,[1,2,4] Dominik Kriegner,[5] Václav Holý,[5]
Přemysl Beran,[6] Easo P. George,[7,*] Jörg Neugebauer,[8] and Antonín Dlouhý[1]
[1]*Institute of Physics of Materials, Academy of Sciences of the Czech Republic, v.v.i., Žižkova 22, CZ-61662 Brno, Czech Republic*
[2]*Central European Institute of Technology, CEITEC MU, Masaryk University, Kamenice 5, CZ-62500 Brno, Czech Republic*
[3]*Department of Physical Metallurgy and Materials Testing, Montanuniversität Leoben, Franz-Josef-Str. 18, A-8700 Leoben, Austria*
[4]*Department of Chemistry, Faculty of Science, Masaryk University, Kotlářská 2, CZ-61137 Brno, Czech Republic*
[5]*Faculty of Mathematics and Physics, Charles University, Ke Karlovu 5, CZ-12116 Prague 2, Czech Republic*
[6]*Nuclear Physics Institute, Academy of Sciences of the Czech Republic, Řež 130, CZ-25068 Husinec, Czech Republic*
[7]*Institute for Materials, Ruhr University, D-44801 Bochum, Germany*
[8]*Max-Planck-Institut für Eisenforschung GmbH, D-40237 Düsseldorf, Germany*

(Received 27 January 2017; revised manuscript received 15 May 2017; published 28 July 2017)

We present experimental data showing that the equiatomic CrMnFeCoNi high-entropy alloy undergoes two magnetic transformations at temperatures below 100 K while maintaining its fcc structure down to 3 K. The first transition, paramagnetic to spin glass, was detected at 93 K and the second transition of the ferromagnetic type occurred at 38 K. Field-assisted cooling below 38 K resulted in a systematic vertical shift of the hysteresis curves. Strength and direction of the associated magnetization bias was proportional to the strength and direction of the cooling field and shows a linear dependence with a slope of 0.006 ± 0.001 emu/T. The local magnetic moments of individual atoms in the CrMnFeCoNi quinary fcc random solid solution were investigated by *ab initio* (electronic density functional theory) calculations. Results of the numerical analysis suggest that, irrespective of the initial configuration of local magnetic moments, the magnetic moments associated with Cr atoms align antiferromagnetically with respect to a cumulative magnetic moment of their first coordination shell. The *ab initio* calculations further showed that the magnetic moments of Fe and Mn atoms remain strong (between 1.5 and 2 μ_B), while the local moments of Ni atoms effectively vanish. These results indicate that interactions of Mn- and/or Fe-located moments with the surrounding magnetic structure account for the observed macroscopic magnetization bias.

DOI: 10.1103/PhysRevB.96.014437

I. INTRODUCTION

Equiatomic compositions maximize the configurational entropy of random solid solutions [1]. Yeh and co-authors [2] built on this principle and suggested that, when five or more elements combine in equiatomic proportions, the configurational entropy contribution to Gibbs free energy may be sufficient to overcome competing thermodynamic forces and provide stability to a single-phase microstructure. Alloys consisting of multiple principal elements in approximately equiatomic concentrations have been termed high (configurational) entropy alloys (HEAs). HEAs are intriguing since certain combinations of elements in a single phase may exhibit a number of unusual physical properties with high potential for applications [3]. Consequently, complex alloy systems with nearly equiatomic composition [compositionally complex alloys (CCAs)] have been the subject of rapidly increasing research in the past decade; see, e.g., Refs. [4–11]. Many experimental, e.g., Refs. [7,12], and computational, e.g., Refs. [13,14], studies have provided evidence that the configurational entropy term is usually insufficient to stabilize CCAs as a single phase. Contrary to the hypothesis of Yeh *et al.* [2], phase separation of the investigated CCAs is rather the rule than the exception. However, a few systems have been found that seemingly obey the original HEA principle. The single-phase equiatomic Cantor alloy CrMnFeCoNi [15], which crystallizes in a face centered cubic (fcc) lattice, is one of the best-known examples. While it can decompose into multiple phases when annealed at temperatures below about 1073 K [16–18], it can also be produced as a single-phase fcc material in the cast, homogenized, and recrystallized states. After hot or cold deformation processing and subsequent recrystallization of the material, the single-phase CrMnFeCoNi alloy exhibits certain unusual properties such as a good combination of strength and ductility, both of which increase with decreasing temperature [19,20], and a remarkably high fracture toughness [21].

A review of the magnetic and electrical properties of HEAs was recently published by Tsai [22]. The studies of magnetic properties of HEAs were mainly focused on the alloys composed of Al, Co, Cr, Cu, Fe, Ni, and Ti [23–31]. These alloys usually contain more than 50 at.% of the magnetic elements—Fe, Co, and Ni—and they are either paramagnetic [25,27,30] or ferromagnetic and their saturation magnetization depends mainly on the composition and crystal structure. In general, more magnetic elements lead to higher magnetization [22,31]. However, other alloying elements can also have an impact, e.g., addition of Cr significantly reduces the magnetization [22,31]. Zhang *et al.* [31] have argued that this is because the magnetic moments of Cr atoms have an antiparallel orientation to moments of Fe/Co/Ni leading to reduction of the total magnetization of the alloy [31]. This

---

[*] Currently at Oak Ridge National Laboratory, Oak Ridge, TN 37831, USA and University of Tennessee, Knoxville, TN 37996, USA.

2469-9950/2017/96(1)/014437(13)

explanation was supported by *ab initio* investigations on the CrMnFeCoNi alloy [32]. It should be mentioned that magnetic hardening of FeCr and FeCrCo alloys, which is associated with the formation of a two-phase microstructure on the nanometer scale, has been investigated in detail in the past [33–35]. It was found that a modulated structure consisting of Fe-rich and Cr-rich regions is formed via spinodal decomposition in these alloys.

In spite of the fact that, out of the five elements in the Cantor alloy, three elements namely Ni, Co, and Fe are ferromagnetic in their standard conditions, there are only scarce data concerning the magnetic properties of this HEA. Recently, Ji *et al.* [36] and Yu *et al.* [37] reported on a paramagnetic type of the magnetization curve recorded at room temperature for CrMnFeCoNi fine powders consolidated by either spark plasma or high pressure sintering. Jin and co-workers [38] investigated electrical resistivity, thermal conductivity, and magnetization of eight Ni-based, face-center-cubic (fcc) equiatomic alloys including the quinary high entropy CrMnFeCoNi alloy. Their magnetization-temperature data suggest that spin glass may form in the CrMnFeCoNi alloy below 25 K; however, no additional evidence was provided in their paper to support this conclusion. In summary, a systematic experimental study of the magnetic properties of the CoCrFeMnNi alloy is lacking.

On the basis of computational studies, Ma and co-workers [39] investigated thermodynamic properties of the Cantor alloy taking into account all the relevant free energy contributions including magnetic excitations. They used an exact muffin-tin orbitals (EMTO) method within a framework of the density functional theory (DFT) and, based on their calculations, predicted a paramagnetic to ferromagnetic transition at about 20 K. Experimental data, which would either confirm or disprove this prediction, do not exist. To resolve these open issues and to obtain a deeper insight into the role of magnetism in this alloy we performed a combined experimental and computational study.

II. EXPERIMENTS AND COMPUTATIONAL METHODS

A. Material

The equiatomic alloy CrMnFeCoNi was arc-melted and drop cast under pure Ar atmosphere using raw materials with purity of at least 99.9%, similar to the process described in previous publications [12,20,40]. Prior to melting, the chamber was evacuated to 7×10^{-4} Pa and then backfilled with Ar gas to a pressure of 8.4×10^{-4} Pa. A small piece of Zr was first melted to getter any residual oxygen that might be present in the chamber. The arc-melted buttons were flipped and remelted five times to thoroughly mix the elements before the molten alloy was dropped into a rectangular Cu mold. The rectangular drop-cast ingots ($127\times25.4\times12.7$ mm^3) were cleaned in an aqueous solution of hydrochloric acid and hydrogen peroxide, encapsulated in evacuated quartz ampoules and homogenized for 48 h at 1473 K. The ingots were subsequently cold rolled along the longitudinal ingot direction to ~27 mm wide slabs. The final thickness of the slabs was either 6 or 4 mm, that is, a reduction in thickness of 53% or 69%, respectively. The rolled slabs were subsequently annealed for 1 h at 1173 K to obtain a fully recrystallized equiaxed microstructure with a grain size of 36 ± 6 μm. Specimens for structure analysis and measurements of magnetic properties were cut from the (recrystallized) slabs using the spark erosion technique.

B. Structure analysis and magnetic measurements

Structure and phase composition were examined by x-ray and neutron powder diffraction. X-ray diffraction measurements were performed in Bragg Brentano geometry with a linear detector [41] in the temperature range of 3 to 300 K using CuK_α radiation. The data were analyzed using the Cohen-Wagner plot to obtain the temperature dependence of the lattice parameter. Neutron powder diffraction measurements were carried out on MEREDIT diffractometer (Institute of Nuclear Physics AS CR Rez in the Czech Republic) in the temperature range 4–300 K. ^{57}Fe Mössbauer spectroscopy was used for phase and magnetic analysis. This was carried out in transmission geometry with detection of 14.4 keV gamma radiation. The spectra were measured in the temperature range 5–293 K and calibrated against α-Fe. Two different experimental setups were employed, one for measurements in low external magnetic fields (up to 300 Oe) and the other for the data acquisition at the external field of 50 kOe. Computer processing of the spectra was done using the CONFIT program package [42].

Magnetic measurements were carried out using PPMS—Physical Property Measurement System EverCool II (2–400 K; 0–9 T) with vibrating sample magnetometer. Temperature dependences of the magnetic moment were investigated in the temperature range 5–380 K. The temperature dependences of magnetic moment were measured after zero field cooling (ZFC) or after cooling in a magnetic field (FC) of various strengths. Subsequently, the magnetic moment of the sample was recorded during the heating part of the temperature cycle using a heating rate of 2 K/min. The samples were subjected to external fields ranging from 0 to 500 Oe during heating. Similarly, field dependencies of the magnetic moment were measured in the same temperature range while varying the external field between ±1 T. Additionally, measurements of electrical resistivity and magnetoresistance were performed in order to further characterize electronic properties of the investigated HEA. These measurements were carried out in the temperature range 5–300 K (0–9 T) with the four-point method. A strip-shaped sample with dimensions $10\times2\times0.02$ mm was undulated to fit the sample holder and the external magnetic field was oriented parallel to the width (2 mm) of the strip during the measurements.

C. Computational methods

Our quantum-mechanical (so-called *ab initio*) calculations were performed within the framework of density functional theory [43,44] using the Vienna Ab initio Simulation Package (VASP) [45,46] and projector augmented wave pseudopotentials [47,48]. The exchange and correlation energy was treated in the generalized gradient approximation as parametrized by Perdew, Burke, and Ernzerhof [49]. We used a plane-wave energy cutoff of 350 eV with a $6\times4\times4$ Monkhorst-Pack k-point mesh. Our 90-atom fcc-based computational supercell

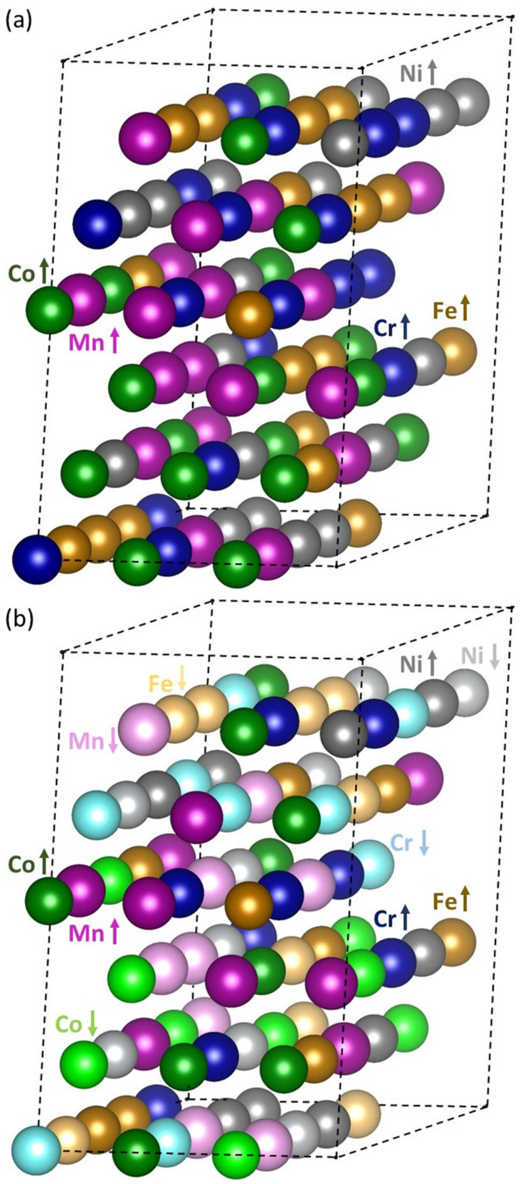

FIG. 1. Schematic visualization of the 90-atom computational supercells used for our quantum-mechanical calculations with (a) all local magnetic moments of Cr, Mn, Fe, Co, and Ni atoms initially (before the full relaxation) oriented in a parallel manner in a ferromagnetic state and (b) half of the local magnetic moments within each element's sublattice initially oriented in an antiparallel manner (simulating a paramagnetic state) while the total magnetic moment is zero and is kept zero during the relaxation.

was built upon (111) basal planes with cell vectors along the [$\bar{1}10$], [$\bar{1}\bar{1}2$] and [111] crystallographic directions; see Fig. 1.

The supercell contained 18 atoms of each of the five chemical elements, Cr, Mn, Fe, Co, and Ni. The atoms were distributed according to the special quasirandom structure (SQS) concept [50] to model their random distribution over the fcc lattice sites. We also included "up" or "down" (parallel or antiparallel) orientation of their magnetic moments. The calculations considered two distinct configurations.

In the first case, the initial parallel (e.g., up) orientation of all local magnetic moments carried by Cr, Mn, Fe, Co, and Ni atoms simulated a ferromagnetic state. A subsequent minimization of the total energy with respect to the supercell volume, its shape, atomic positions, and all electronic degrees of freedom (a full relaxation) reduced forces acting on individual atoms below 1 meV/Å and changed the values as well as orientations of local magnetic moments (the final state was not ferromagnetic; see below). In the second situation, the initial orientation of local magnetic moments emulated the paramagnetic state. Thus the initial magnetic moments within each of the five sublattices were set antiparallel to each other (nine moments up and nine moments down in each element sublattice). In this case, the overall (total) magnetic moment of the computational supercell was constrained to zero during the energy minimization process.

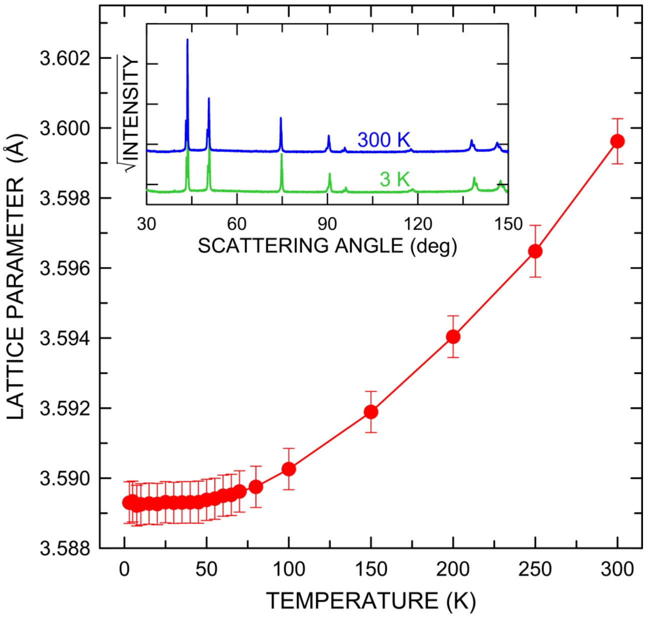

FIG. 2. Temperature dependence of the lattice parameter determined by x-ray diffraction. The inset shows the measured x-ray diffraction pattern at 3 and 300 K. Curves in the inset are vertically shifted for clarity.

III. RESULTS

XRD results shown in Fig. 2 indicate that the structure of the investigated HEA remains fcc down to a temperature of 3 K. The decrease in the lattice parameter with decreasing temperature saturates below 50 K. Neutron diffraction experiments yielded temperature dependences of the {111} and {222} interplanar spacings. They are summarized in Fig. 3 and confirm the results of XRD measurements both with respect to the lattice parameter decrease and its saturation. Neutron diffraction did not detect any long range ordering of magnetic moments.

The temperature dependencies of the magnetic moment recorded during cooling-heating cycles in the temperature range between 5 and 300 K are shown in Figs. 4 and 5. A zero field cooling (ZFC) yielded the blue curve in Fig. 4 which documents first an increase (temperatures between 300 and 100 K) and subsequent saturation of the magnetic moment (temperatures below 100 K) with a small jump at 40 K.

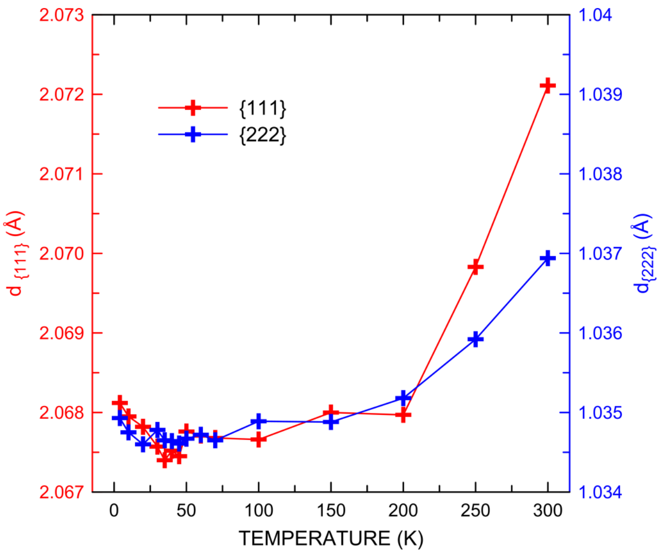

FIG. 3. Temperature dependence of {111} and {222} cell parameters derived from the neutron diffraction data.

Similar small jumps in magnetization were also recorded at 40 K during the heating part of the cycles carried out in an external field of 100 Oe; see red and green curves in Fig. 4. These dependencies were obtained after zero-field cooling (ZFC, red curve) and 5 T field cooling (FC, green curve). The present results suggest that the investigated HEA undergoes two magnetic transitions, first at the start of the saturation plateau at about 90 K and second at the position of the magnetization jumps at 40 K. Further experimental evidence confirming the two transitions was obtained after ZFC when the samples were heated in different external fields of 50, 100, 200, and 500 Oe; see Fig. 5. The charts shown in Fig. 5 allowed us to pin down the transition temperatures more accurately as 93 K and 38 K for the first and second transition, respectively.

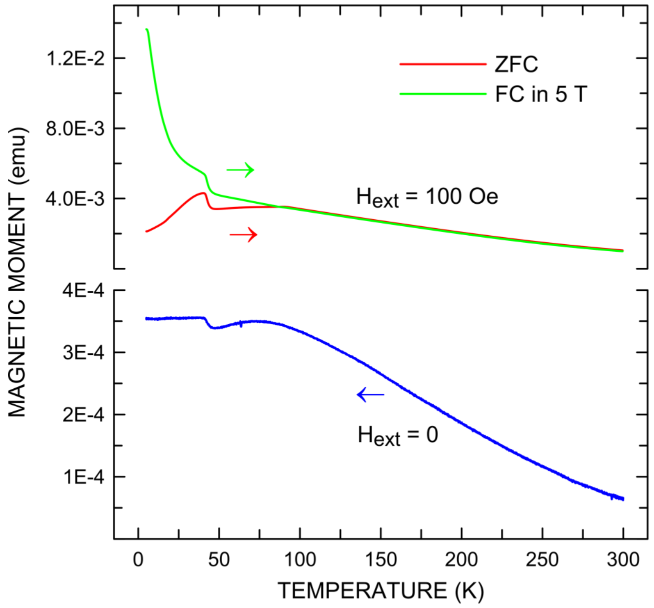

FIG. 4. Temperature dependence of magnetic moment measured with decreasing temperature in zero field (blue data points), with increasing temperature after zero field cooling in 100 Oe, and with increasing temperature after 5 T (green data points) field cooling in 100 Oe.

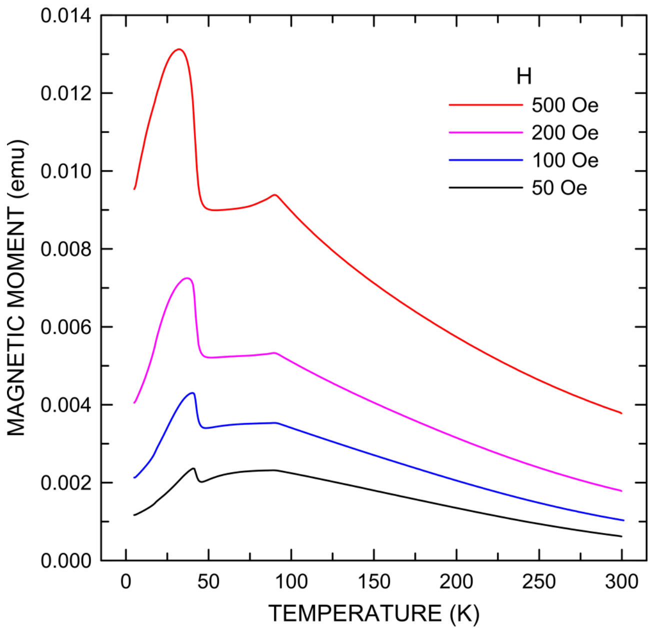

FIG. 5. Temperature dependencies of magnetic moment measured after zero field cooling with increasing temperature in 50, 100, 200, and 500 Oe magnetic field.

The transitions were further confirmed by the field dependences of the magnetic moment shown in Fig. 6. While after ZFC to temperatures between room temperature and 120 K the mostly linear magnetization curves correspond to the paramagnetic state of the alloy [Fig. 6(a)], subtle hysteresis loops (HLs) were recorded after ZFC below 40 K [Fig. 6(b)]. We suggest that the critical point on ZFC curves at 93 K shown in Fig. 5 and the maximum of dc susceptibility (dM/dH) at the same temperature documented in Fig. 7 can be attributed to the transition between the paramagnetic state and a spin glass which freezes at $T_g = 93$ K. The nature of this spin-glass transition is clearly demonstrated in Fig. 8 which shows a relaxation of the magnetic moment with increasing time after field cooling (FC) to temperatures below 90 K. Schematic charts in Fig. 8(a) explain the thermal and external magnetic field history prior to the measurement of the relaxation curves.

The samples were cooled to 70 K (below the spin-glass transition temperature T_g) under an external field of 100 Oe. Once the final temperature of 70 K was reached, the field was kept at the original level for an additional waiting period t_w after which the field was switched off and the relaxation process started. Waiting periods t_w of 600, 1800, and 7200 s have only a weak effect on the relaxation process as can be inferred from the relaxation curves shown in Fig. 8(b). The shortest investigated waiting period of 600 s resulted in magnetic moments that were slightly but systematically smaller than the moments measured after the other two waiting periods. In all three experiments the magnetic moment of the sample vanished after relaxation times t_m of the order of 10^4 s.

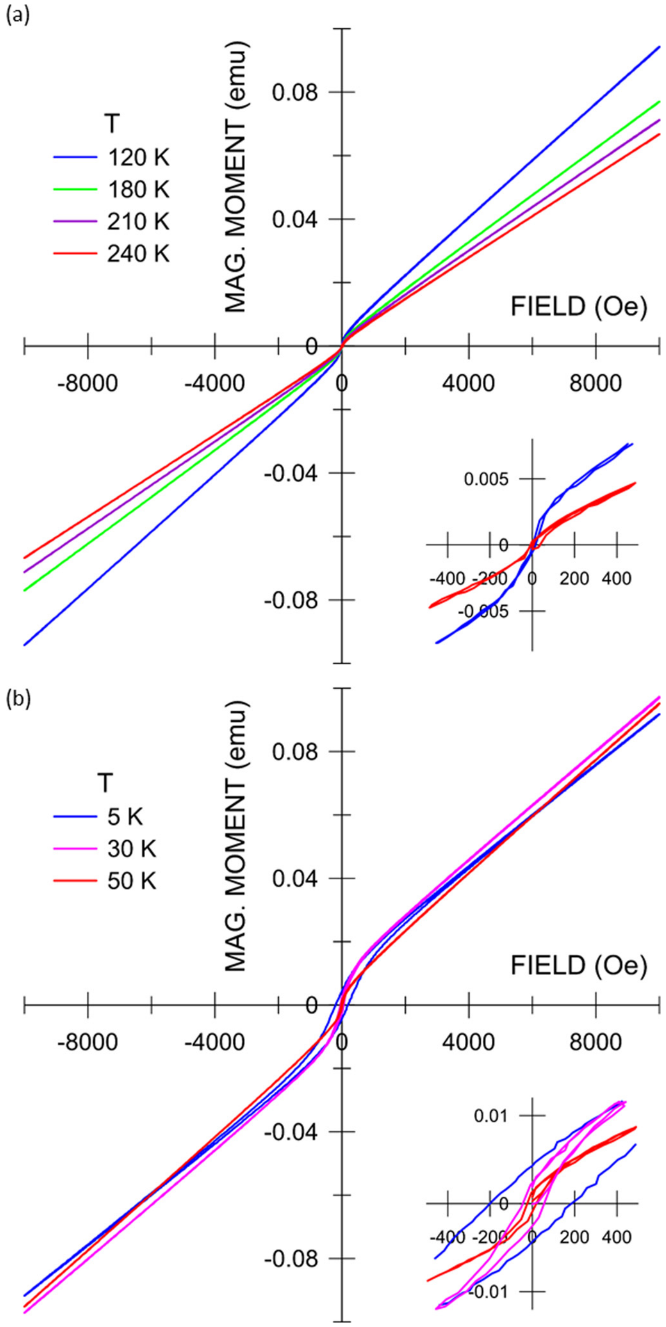

FIG. 6. Field dependence of magnetic moment at 120, 180, 210, and 240 K after zero field cooling (a). Field dependence of magnetic moment at 5, 30, and 50 K after zero field cooling (b).

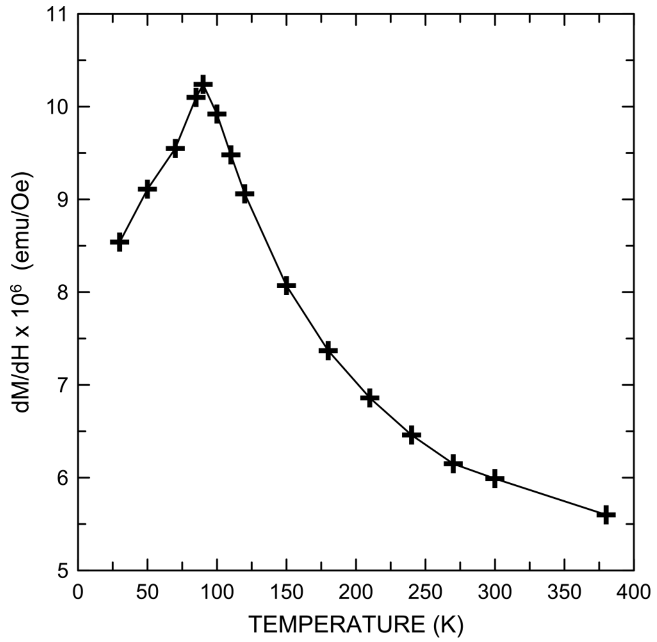

FIG. 7. Temperature dependence of dc susceptibility dM/dH.

In order to assess the character of the second magnetic transition at 38 K, the following additional experiments were carried out. First, HLs were recorded after FC in $+5$ or -5 T down to 5 K and a striking result was obtained. As shown in Fig. 9, the corresponding HLs exhibit a uniform shift in magnetization (vertical shift) in a direction governed by the orientation of the cooling field. The magnitude of the shift changes with the strengths of the external field applied during cooling and can be estimated as 0.006 ± 0.001 emu/T. In Fig. 9, the shifted HLs are compared with a HL which was recorded after ZFC and which follows a normal path centered on a point of zero field and magnetization. In the next experiment, the alloy was first subjected to ZFC cooling down to 70 K (temperature below the first magnetic transition), followed by FC with ± 5 T to 5 K.

After this cooling path, the HLs measured at 5 K exhibited the same behavior as that shown in Fig. 9. In the last experiment, the FC with ± 5 T stopped at 70 K and magnetization curves were recorded at this temperature. Here, neither was any hysteresis present nor any shift observed with respect to the ZFC state; see Fig. 10. These additional results provide clear evidence that the second transition is of a ferromagnetic type and may be associated with local ordering of magnetic moments on Fe, Co, and/or Mn atoms. Further work is required to clarify this point. In this respect, Mössbauer spectroscopy can provide an important insight into the magnetic arrangements in the surroundings of the Fe atoms. The Mössbauer spectra measured at 5 K in external fields ranging from 0 to 50 kOe are presented in Fig. 11.

The Mössbauer spectrum taken at room temperature is represented by a single line with isomer shift (relative to pure α-Fe) $\delta = -0.091 \pm 0.010$ m/s corresponding to a paramagnetic material. The value of δ is in agreement with that for fine gamma iron, e.g., in the form of precipitates in Cu rich CuFe alloys [51,52]. An important broadening of the single line can be observed at 5 K [Fig. 11(a)]. The spectrum acquired at 5 K and a zero external field was fitted by the sextet with hyperfine induction $B_{\mathrm{hf}} = 4.43$ T with a Gaussian hyperfine distribution $\Delta w = 5.23$ T using a linewidth $\Gamma = 0.35$ mm/s. An intensity ratio of the second to the first line in the sextets was $R_{21} = 1.1$. This result suggests that the orientation of the Fe moments was preferentially perpendicular to the gamma beam propagation. The spectrum measured at 5 K in the external magnetic field 300 Oe (parallel to the gamma beam) exhibited a slight increase in B_{hf} to 5.43 T with $\Delta w = 8.39$ T and $R_{21} = 1.1$ The fitting parameters of the spectrum measured in

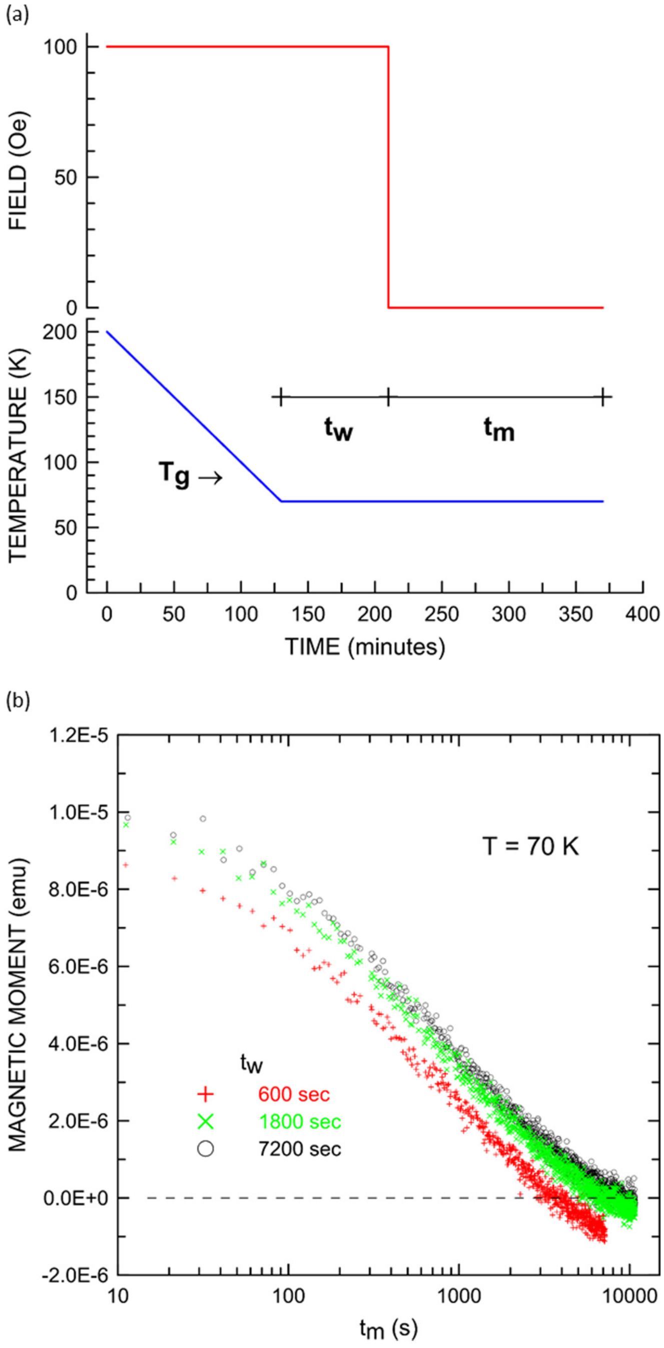

FIG. 8. Sketch of the relaxation measurement procedure (a). Relaxations of magnetic moment for various waiting times t_w at 70 K (b).

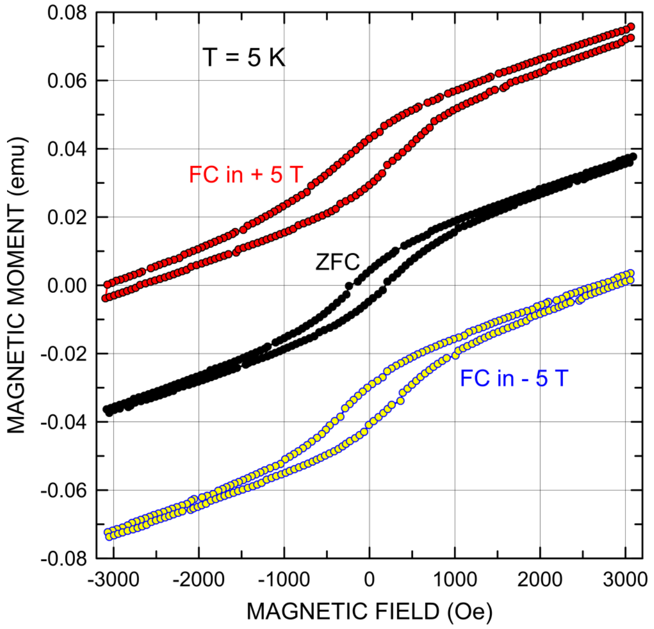

FIG. 9. Magnetic moment vs magnetic field measured at 5 K after zero field cooling (ZFC) and field cooling in +5 T and −5 T.

the external field 50 kOe were $B_{\text{hf}} = 6.04$ T, $\Delta w = 5.77$ T, and $R_{21} = 1.33$ [Fig. 11(b)]. These fitting results would be consistent with a persisting arrangement of the Fe moments which are still nearly perpendicular to the external field (the gamma beam direction). Moreover, a contribution due to an antiferromagnetic ordering of the moments surrounding the Fe atoms combined with a perpendicular ferromagnetic component may contribute to the shape of the spectra acquired at high external fields [53]. A similar arrangement of moments can also account for the magnetic data presented in Fig. 5. No difference in the spectra measured in the external field 50 kOe at 5 K was found when the external field was either switched off during cooling from room temperature (green points in Fig. 11) or was assisting the whole cooling path down to 5 K [orange points in Fig. 11(b)].

Measurements of electrical resistivity and magnetoresistance are important since they may support or disprove our inference of two magnetic transitions. A detected temperature dependence of the relative resistivity $R(T)/R(300)$ is shown in Fig. 12. The linear part at high temperatures (above 150 K) is followed by a minimum of relative resistivity at about 30 K and

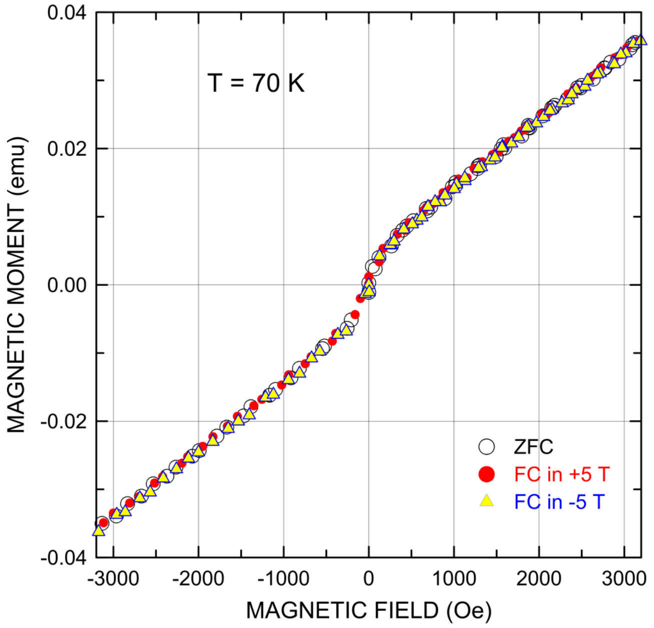

FIG. 10. Magnetic moment vs magnetic field measured at 70 K after ZFC and field cooling in +5 T and −5 T.

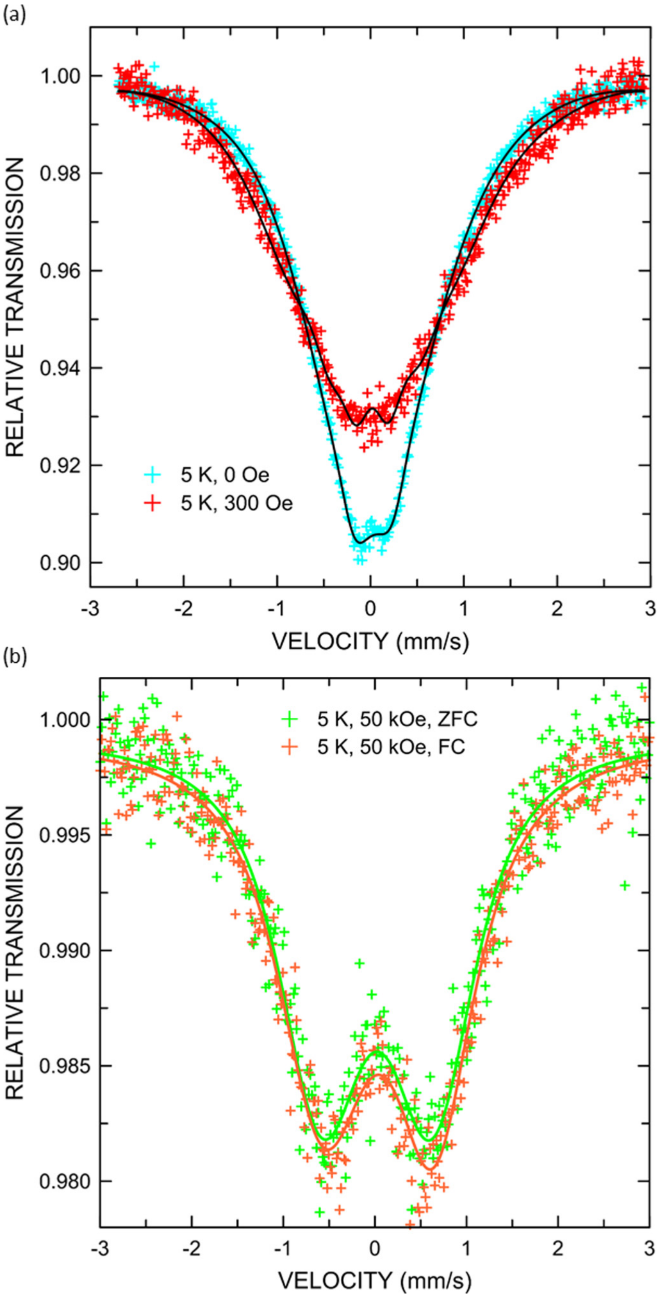

FIG. 11. Mössbauer spectra taken at 5 K with and without external magnetic field. (a) Measurements were assisted by external magnetic fields 0 and 300 Oe. (b) Measurements were assisted by external magnetic fields 50 kOe. The green data were acquired after ZFC; the orange data correspond to magnetic state established after FC with 50 kOe. The smooth curves were fitted to the individual experimental data sets using the CONFIT program [42].

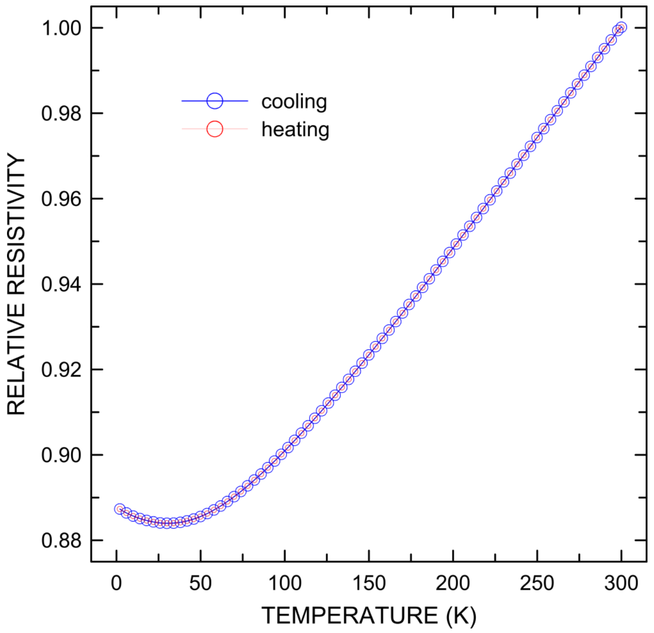

FIG. 12. Temperature dependence of relative electrical resistivity $R(T)/R(300)$ without external magnetic field.

then the relative resistivity increases with further cooling. A similar temperature dependence of the resistivity was obtained in an external magnetic field of 5 T. This dependence is plotted as the red curve in Fig. 13. Blue circles in Fig. 13 represent differences $|R(5\text{ T}) - R(0\text{ T})|$ in the resistivity measured in an external field of 5 T and the zero external field. These differences reflect variations in strength of the interaction between itinerant electrons and the local magnetic order induced by the strong external field. As expected, the differences $|R(5\text{ T}) - R(0\text{ T})|$ increase with decreasing temperature in the paramagnetic regime down to about 90 K, while in the spin glass range they drop to zero at about 40 K and, finally, they again increase sharply with the ferromagnetic ordering in the temperature range below 40 K. Similarly, magnetoresistance defined by relation $\Delta R = [R(H) - R(0)]/R(0)$ was investigated in external magnetic fields H between -5 T and $+5$ T in a temperature range 2–100 K (see the results in Fig. 14).

Analogous to the resistivity differences plotted in Fig. 13, the results shown in Fig. 14 suggest that there is a clear change

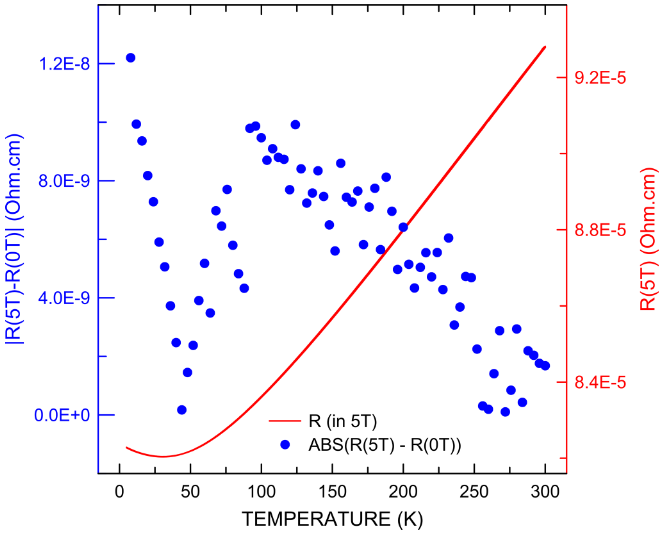

FIG. 13. Temperature dependence of electrical resistivity in external magnetic field 5 T (red line) and the absolute value of the difference between the measurements in 0 T and 5 T (blue circles).

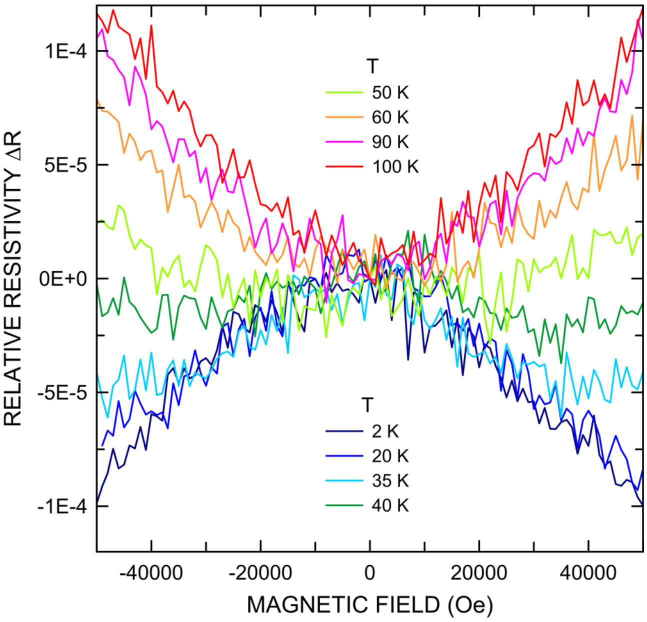

FIG. 14. Magnetoresistance at various temperatures.

in the shape of the curves at around 40 K. The two branches of the magnetoresistance curves were separately fitted in intervals -5 T to 0 and 0 to $+5$ T by linear functions and their slopes $|\Delta R/\Delta H|$ plotted as a function of temperature in Fig. 15.

Similar to the $|R(5\text{ T}) - R(0\text{ T})|$ results presented in Fig. 13, the data in Fig. 15 exhibit two extremes, a sharp minimum at ≈40 K and a maximum at 90 K. The temperatures of the maximum and the minimum of the dependencies presented in Figs. 13 and 15 correspond to the transition temperatures observed on the temperature dependencies of the magnetic moment; see Figs. 4 and 5. An increase in $|R(5\text{ T}) - R(0\text{ T})|$ differences in Fig. 13 and the increase in the slopes in Fig. 15 below the critical temperature 40 K can be explained as the effect of impurities atoms which do not participate in the basic ferromagnetic ordering as discussed in Ref. [54].

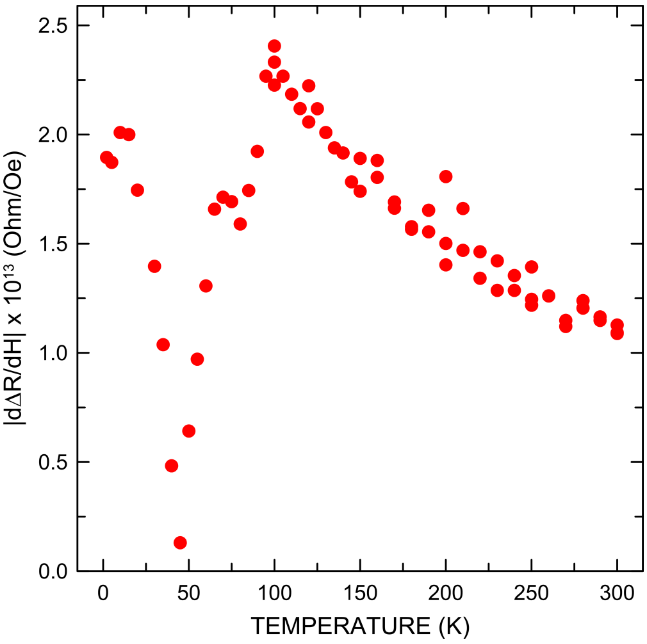

FIG. 15. Changes of magnetoresistance slope at various temperatures.

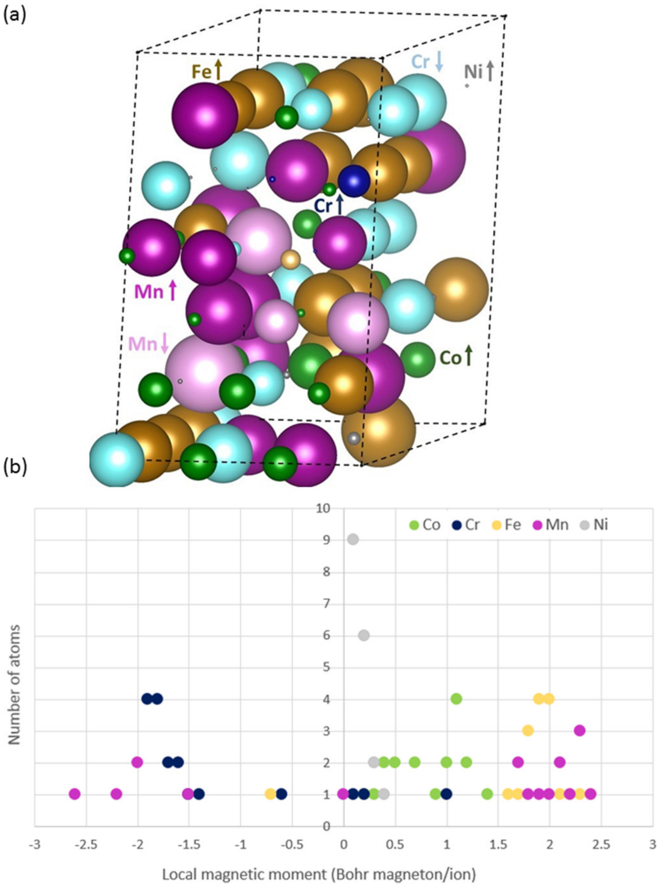

FIG. 16. Schematic visualization (a) of the quantum-mechanically computed local atomic magnetic moments in the 90-atom computational supercell after a full optimization. The magnitude of the local moments is depicted by the size of the corresponding atomic spheres. Some local magnetic moments reversed their orientation to an antiparallel one (with respect to the initial parallel orientation) and these are shown by brighter colors [compared with those used in Fig. 1(a)]. In particular, Mn atoms with the original orientation are depicted by darker violet color while those with the antiparallel orientation are shown by lighter violet color. Cr atoms with antiparallel orientation of the local magnetic moments are depicted by light blue color (only one Cr atom kept the initial orientation of the local magnetic moment and it is shown by a darker-blue sphere). One Fe atom also reoriented its magnetic moment and it is shown as a small lighter-brown sphere close to the center of the cell. Element-resolved distributions (b) of the values of local magnetic moments in the final quantum-mechanically computed state depicted in part (a) [negative values indicate antiparallel orientation of the final moments with respect to the initial one seen in Fig. 1(a)].

Results of our *ab initio* calculations are summarized in Figs. 16 and 17. The full relaxation of the initial ferromagnetic arrangement (IFMA) yielded the data shown in Fig. 16. In Fig. 16(a), the magnitude of the local magnetic moments

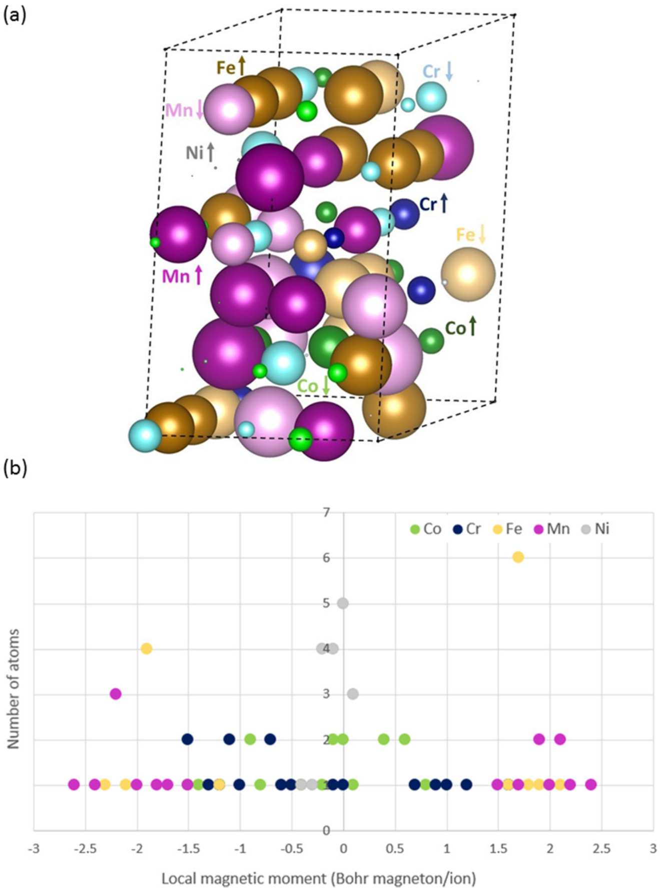

FIG. 17. (a) Same as in Fig. 16 but for the initially antiparallel orientation of local magnetic moments [see Fig. 1(b)].

after relaxation is represented by the size of the spheres at the positions of the individual atoms. During the total energy minimization, some of the local magnetic moments flipped in an opposite direction with respect to their starting orientation. These re-orientation events are indicated by lighter colors in Fig. 16(a). The flipping took place for most of the Cr atoms (15 out of 18), some of the Mn atoms (5 out of 18), and only once for a Fe atom. In the total energy minimum configuration, almost all Ni atoms exhibit surprisingly low magnetic moments. These moments are less than 0.25 μ_{B}. Significant reductions are observed also for the majority of the Co atoms, for two Cr atoms, and one of the Mn atoms (the latter is practically nonmagnetic). Element-resolved distributions of the local magnetic moments, which correspond to the state presented in Fig. 16(a), are shown in Fig. 16(b). The net total magnetic moment of the whole cell is 45.2 μ_{B}, i.e., on average, only 0.5 μ_{B} per atom. Similar results obtained after the full relaxation of the initial antiferromagnetic arrangement (IAMA) are shown in Fig. 17. Here the overall magnetic moment of the supercell was constrained to zero during the total energy minimization. The initial local magnetic moments were oriented in an antiparallel manner within each element sublattice. Magnetic moments carried by the individual atoms are again represented in Fig. 17(a) by the size of atomic spheres with the same color coding as in Fig. 16(a).

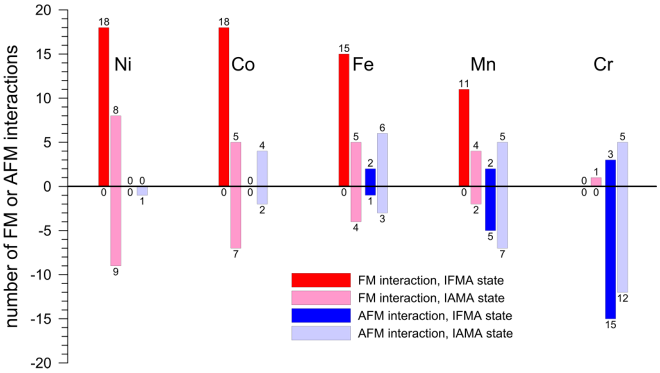

FIG. 18. Number of FM and AFM interactions between a central atom and its first coordination shell sorted according to the chemistry of the central atoms and the sign of the central magnetic moment (plus for "up" and minus for "down" orientation). Red and blue columns represent, respectively, the number of ferromagnetic and antiferromagnetic interactions in the initial ferromagnetic arrangement (IFMA) state while light red and light blue columns correspond to similar frequencies in the initial antiferromagnetic arrangement (IAMA) state; see text for details.

The low energy configurations obtained by our *ab initio* calculations are analyzed further with a special focus on the local magnetic arrangements in the first coordination shell around a given central atom. We first sum up all magnetic moments in the first coordination shell of one selected atom. Unless the sum has a zero value, this cumulative moment can be oriented either up or down. The orientation of the cumulative moment is then compared to the orientation of the magnetic moment carried by the central atom. The character of the exchange between the central atom and its first coordination shell is considered ferromagnetic when the central and cumulative moments are parallel.

Conversely, when these two moments are antiparallel, the interaction is antiferromagnetic. Recalling that the computational supercell contains 18 atoms that belong to one of the five chemical components, the exchange interactions can thus be expressed according to the chemical nature of the central atoms. Final results, based on the analysis of the IFMA and IAMA low energy states, are plotted in Fig. 18 as a bar chart. Here red and blue columns represent, respectively, the number of ferromagnetic and antiferromagnetic interactions in the IFMA state, while light red and light blue columns correspond to similar frequencies in the IAMA state. These results suggest that the central Ni and Co atoms exhibit almost exclusively ferromagnetic interactions with their surroundings. Fe and Mn atoms may also show antiferromagnetic exchanges in a statistically relevant number of cases, particularly in the IAMA case. On the other hand, Cr central atoms prefer almost exclusively antiferromagnetic arrangements, irrespective of the initial configuration.

IV. DISCUSSION

Our XRD and neutron-diffraction structure analysis of the CoCrFeMnNi high-entropy alloy confirms a single phase fcc structure down to a temperature of 3 K. These diffraction techniques did not provide any evidence for even local volumes occupied by other crystallographic structures, e.g., by tetragonal, B2, or bcc phases as recently reported by Otto and co-workers [18] after long-term, intermediate-temperature anneals. We also do not observe any transition to the hcp structure predicted by previous EMTO calculations [39].

However, our XRD and ND results must be interpreted with care since the coherent scattering length of the potential secondary phases in their embryonic stages may fall below the resolution limit of the applied diffraction techniques [55]. In this context, it is worth noting that the lattice parameter of the investigated HEA saturates at about 3.59 Å which is very close to the lattice parameter reported for fcc iron precipitates in Cu [56] or fcc iron investigated at high pressures [57].

Temperature dependencies of the total magnetic moment of the sample reveal two magnetic transitions at 93 and 38 K; see Fig. 5. Experimental data presented in this study strongly suggest that the spin/superspin glass freezes at $T_g = 93$ K. The formation of a (super)spin glass state below 93 K is in line with the temperature dependence of the magnetic susceptibility (Fig. 7) and leads to a magnetic moment relaxation at temperatures below the freezing point [see Fig. 8(b)]. The relaxation processes exhibit characteristics fully consistent with the behavior of spin glasses described in earlier studies; see, e.g., Ref. [58]. The regime below the second transition temperature at 38 K is associated with a sharp increase of the sample magnetic moment with decreasing temperature and the development of HLs [Figs. 5 and 6(b)]. This behavior can be attributed to a ferromagnetic ordering of at least a part of the local magnetic moments. At present, it is not clear which atoms or atomic clusters contribute to this phenomenon and additional studies are required to clarify this point. In addition, the two mentioned transitions were confirmed by measurements of electrical resistivity and magnetoresistance in the respective temperature regimes; see Figs. 12–15. Interestingly, the sequence of paramagnetic → (super)spin glass → ferromagnetic regimes observed with decreasing temperature in this study for equiatomic quinary CoCrFeMnNi alloy differs from the paramagnetic → ferromagnetic → (super)spin glass order found recently for the ternary $Cr_{23}Fe_4Ni_{73}$ alloy [59]. Apparently, the two low-temperature regimes swap when the compositional complexity of the alloy increases.

Furthermore, the field assisted cooling of CoCrFeMnNi below 40 K results in a systematic vertical shift of HLs in the direction consistent with the polarity of external field applied during FC; see Fig. 9. In the case of a random fcc solid solution, this is a rather unexpected and new phenomenon. A similar vertical shift of HLs was recently observed in an AF martensitic Heusler alloy $Ni_{50}Mn_{45}In_5$ and interpreted as a shell-ferromagnetism associated with the $Ni_{50}Mn_{45}In_{25}$ precipitation in the $Ni_{50}Mn_{50}$ matrix [60]. The shift of HLs reported in the present study is purely vertical (in the direction of the magnetization axis) without any component parallel to the field axis. This is different from the exchange bias effects observed either in nanoparticles with radial ferromagnetic core–antiferromagnetic shell structures or in nanosandwiches composed of ferromagnetic-antiferromagnetic nanolayers [61–63]. Since none of the mentioned nanostructures is present in the investigated CoCrFeMnNi alloy, it may be expected that the effect stems from ordering of magnetic moments carried by specific atoms in concert with the arrangements of atomic moments in their nearest neighborhood. It is suggested that an ensemble of these specific clusters represent a magnetically "hard" phase the magnetization of which is set in strong external fields during FC and is extremely difficult to revert in relatively weak magnetic fields during HLs scans. Which atoms/clusters contribute to this effect is a subject of further investigation. This effort may be guided by earlier results on exchange anisotropy reported for binary Mn-X alloys (X = Ni, Co, Fe, Cu, and Ag); see, e.g., Ref. [64]. We thus can conclude that the CoCrFeMnNi alloy has an ability to "remember" the direction of the magnetic field applied on cooling. Finally, we underline again that this "memory" effect is only observed in the temperature range below 40 K and is thus associated with the second transition of the ferromagnetic type.

Our experiments show that the magnetic ordering in the CrMnFeCoNi high-entropy alloy at low temperatures is a complex process. The complexity of the magnetic state has also been confirmed by our quantum-mechanical calculations based on the total energy minimization of the computational supercell using VASP. The calculations leading to this state are computationally very demanding. The computational effort is directly related to the high number of local minima on the Born-Oppenheimer energy surface where many states exist with similar total energies. This situation is best demonstrated when the two sets (IFMA and IAMA) of our *ab initio* data are compared. The difference in energies between the magnetically constrained state at its energy minimum E_{IAMA} (IAMA, corresponding to results in Fig. 17) and the state with fully relaxed energy E_{IFMA} (including fully relaxed magnetic contributions, IFMA—see Figs. 16) was only 10 meV/atom. This rather small energy difference (total energy being higher for the system with the enforced zero total magnetic moment; $E_{\mathrm{IAMA}} > E_{\mathrm{IFMA}}$) indicates that the thermodynamic preference for the fully relaxed state shown in Fig. 16 is very weak and transitions into other magnetic states must be expected. In this respect we can adopt approximations suggested by Ma *et al.* [39] and estimate the transition temperature T_{F} between the state with a zero total magnetization (IAMA—characterized by the energy E_{IAMA}) and the fully relaxed system (IFMA—total energy E_{IFMA}) as $T_{\mathrm{F}} = 2/3(E_{\mathrm{IAMA}} - E_{\mathrm{IFMA}})/k_{\mathrm{B}}$, where k_{B} is Boltzmann constant; see also [65]. This estimate yields the transition temperature $T_{\mathrm{F}} = 77$ K which falls in the range of transition temperatures measured in our experiments.

Our results based on VASP supercell calculations are in good agreement with the predictions of recent DFT studies focused on either the quaternary CoCrFeNi [55] or quinary CoCrFeMnNi [39] HEAs. While numerical methods employed by Ma and co-workers (EMTO) and Niu *et al.* (combined EMTO and VASP) differed from our calculations based fully on SQS and VASP supercell techniques, all three studies predict antiferromagnetic ordering of magnetic moments on Cr atoms with respect to ferromagnetically ordered moments on Fe and Co atoms. In line with our results, the study by Niu and co-authors predicted a considerable reduction of magnetic moments carried by Ni atoms, particularly in combination with $L1_2$-type ordering of Cr atoms. The EMTO calculations by Ma *et al.* [39] also showed that Mn magnetic moments are antiferromagnetically oriented with respect to Fe and Co moments for unit cell volumes slightly higher than the equilibrium volume. Results of our calculations presented in Fig. 16(b) do not fully confirm this type of ordering. After full relaxation of structural and magnetic parameters, only five Mn atoms flipped their magnetic moments into the antiferromagnetic orientation while the remaining 13 Mn atoms kept their original ferromagnetic orientation.

Inspired by the Fe-Cr binary system where a strong repulsion between nearest neighbor Cr atoms exists due to a magnetic frustration of the central Cr atom [66], Niu and co-authors [55] suggested a crystallographic $L1_2$-type ordering of the quaternary CoCrFeNi HEA. In this alloyed $L1_2$ structure, the Cr atoms occupy cube corner positions of the lattice whereas the remaining three ferromagnetic elements are distributed randomly on the face centers and thus form a complete shell of first neighbor ferromagnetic elements around the central antiferromagnetic Cr atom. Calculations by Niu and co-authors provided evidence that this type of Cr ordering results in a considerable reduction of the system free energy. Furthermore, some HRTEM experimental data were presented in support of the scenario suggesting an existence of 2–3 nm ordered domains [55]. A similar scenario can be envisaged also for the quinary CoCrFeMnNi HEA in which magnetic frustration of the antiferromagnetic Cr atoms can be removed by a crystallographic ordering into a A_4B tetragonal-system $I4/m$-type structure (see, e.g., Ni_4Mo data by Casselton and Hume-Rothery [67]). For the equiatomic quinary stoichiometry of the investigated HEA, a distribution of Cr atoms at the corners and the central position of the A_4B tetragonal lattice would provide complete screening of the central antiferromagnetic Cr atom by a first neighbor shell of ferromagnetic atoms Fe, Co, and Ni with the participation of Mn atoms.

However, this Cr screening scenario must be carefully discussed in light of the recent results reported by Otto *et al.* on the decomposition of the quinary CoCrFeMnNi HEA during long-term aging [18]. Their results show that the investigated quinary HEA does not show any sign of decomposition during aging treatments at 1173 K. At an intermediate aging temperature of 973 K, the Cr-rich sigma phase precipitates form and aging at lower temperatures (773 K) results in decomposition into three phases, namely almost pure bcc Cr, tetragonal NiMn, and B2 FeCo. With respect to Cr atoms, the experimentally observed trend is thus just the opposite of the one predicted by the screening scenario; the Cr atoms cluster into Cr-rich sigma phase (approximate composition in at.%: 46Cr, 18Co, 17Fe, 13Mn, and 6Ni) and at lower temperature they form almost pure bcc Cr (86Cr, 4Co, 5Fe, 4Mn, and 1Ni) [18]. In terms of the magnetic contribution to the free energy, these results can be interpreted as a path towards a final antiferromagnetic state of the pure bcc Cr phase. Similar phase separations but into specific Cr-rich nanodomains were reported for Fe-Cr as well as Fe-Cr-Co alloys [33–35]. Interestingly, the same trend can be ascribed to the Mn and Ni atoms, which, at low aging temperature, form the antiferromagnetic $L1_0$ NiMn compound [18,68,69]. We note that relatively high bulk Néel temperatures were reported for Cr (311 K [70]) and MnNi (1073 K [68,69]). High stability of antiferromagnetic Ni-Mn bonds through a broad range of temperatures was also theoretically predicted [71]. Consequently, from the perspective of magnetic contributions to the free energy of quinary CoCrFeMnNi HEA, the experimental data of Otto *et al.* [18] suggest that the alloy prefers to reduce energy by forming antiferromagnetic phases rather than by evolving according to the Cr screening scenario.

In view of the final heat treatment applied in the present work, which resulted in the recrystallization of the quinary CoCrFeMnNi alloy at 1173 K followed by air cooling, we expect very weak tendency towards clustering of the individual atomic species (following the pattern of the alloy decomposition observed experimentally [18]). The tendency to form local bcc, $L1_0$, or $B2$ clusters would be limited mainly due to the sluggish diffusion in the system [11] and the relatively short times available for diffusion during the air cooling step. Nevertheless, based on the experimental results presented in this study, we cannot completely exclude the existence of spatially localized ordered clusters. Further work is needed to clarify this point and its potential relevance for the magnetic characteristics of the quinary CoCrFeMnNi HEA.

V. SUMMARY AND CONCLUSION

We have combined five different experimental methods and DFT-based quantum mechanical calculations in order to characterize magnetic ordering in the quinary CoCrFeMnNi high entropy alloy. Results of our experimental measurements suggest that the system of magnetic moments is in a paramagnetic state down to temperature 93 K. At this freezing point we observe a transition into the (super)spin glass state. The second magnetic transformation of a ferromagnetic type is recorded at 38 K. This transition is likely associated with a ferromagnetic ordering of moments carried by Fe, Co, and/or Mn atoms. The formation of the magnetic order is further confirmed by the measurements of Mössbauer spectra. Field assisted cooling into the ferromagnetic regime below 40 K gives rise to a systematic shift of hysteresis loops in the direction of the magnetization axis (pure vertical shift). The direction of the shift is governed by the polarization of the external field applied during the specimen cooling. XRD and ND data collected between 3 and 300 K provided clear evidence that the alloy remains fcc even though sensitivity of our diffraction techniques may not be sufficient for a detection of nanometer-sized clusters of other crystallographic phases. *Ab initio* calculations showed that the magnetic moments of Fe and Mn atoms remain strong in a range of 1–2 Bohr magneton, while local moments of Ni atoms effectively vanish. Irrespective of the initial configuration of local magnetic moments, the magnetic moments associated with Cr atoms align antiferromagnetically with respect to a cumulative magnetic moment of their first coordination shell. These results indicate that interactions of Mn-located and/or Fe-located moments with the surrounding magnetic structure may account for the observed macroscopic magnetization bias. Further experimental and theoretical effort is required to improve understanding of the magnetic phenomena reported in this study.

ACKNOWLEDGMENTS

This research was supported by the Czech Science Foundation under the Project No. GA14-22834S (A.D., M.F.), by the Academy of Sciences of the Czech Republic [through the Fellowship of J. E. Purkyně (M.F.) and the

Institutional Project No. RVO:68081723 (O.S., M.F., M.D., M.Š., A.D.)], and by the Ministry of Education, Youth and Sports of the Czech Republic under the Projects CEITEC 2020 (LQ1601) (M.F., M.Š.) and the research infrastructure IPMINFRA (LM2015069). E.P.G. acknowledges support from the U.S. Department of Energy, Basic Energy Sciences, Materials Sciences and Engineering Division. D.K. and V.H. acknowledge the support by the project NanoCent financed by European Regional Development Fund (ERDF) (Project CZ.02.1.01/0.0/0.0/15.003/000045). Computational resources were provided by the Ministry of Education, Youth and Sports of the Czech Republic under the Projects CESNET (LM2015042), CERIT-Scientific Cloud (Project No. LM2015085), and IT4Innovations National Supercomputer Center (Project No. LM2015070) within the program Projects of Large Research, Development and Innovations. The computational supercells in Figs. 1, 16(a), and 17(a) were visualized using the VESTA package [72–74].

[1] J. W. Christian, *The Theory of Transformations in Metals and Alloys–Part I* (Pergamon Press, Amsterdam, 2002).
[2] J.-W. Yeh, S. K. Chen, S. J. Lin, J. Y. Gan, T. S. Chin, T. T. Shun, C. H. Tsau, and S. Y. Chang, Adv. Eng. Mater. **6**, 299 (2004).
[3] D. B. Miracle, J. D. Miller, O. N. Senkov, C. Woodward, M. D. Uchic, and J. Tiley, Entropy **16**, 494 (2014).
[4] J. W. Yeh, Ann. Chim. Sci. Mater. **31**, 633 (2006).
[5] Y. J. Zhou, Y. Zhang, F. J. Wang, Y. L. Wang, and G. L. Chen, J. Alloys Compd. **466**, 201 (2008).
[6] O. N. Senkov, G. B. Wilks, D. B. Miracle, C. P. Chuang, and P. K. Liaw, Intermetallics **18**, 1758 (2010).
[7] S. Singh, N. Wanderka, B. S. Murty, U. Glatzel, and J. Banhart, Acta Mater. **59**, 182 (2011).
[8] O. N. Senkov, S. V. Senkova, C. Woodward, and D. B. Miracle, Acta Mater. **61**, 1545 (2013).
[9] J.-W. Yeh, JOM **65**, 1759 (2013).
[10] M.-H. Tsai, K.-Y. Tsai, C.-W. Tsai, C. Lee, C.-C. Juan, and J.-W. Yeh, Mater. Res. Lett. **1**, 207 (2013).
[11] K.-Y. Tsai, M.-H. Tsai, and J.-W. Yeh, Acta Mater. **61**, 4887 (2013).
[12] F. Otto, Y. Yang, H. Bei, and E. P. George, Acta Mater. **61**, 2628 (2013).
[13] W. Cao, Y. A. Chang, J. Zhu, S. Chen, and W. A. Oates, Acta Mater. **53**, 331 (2005).
[14] C. Zhang, F. Zhang, S. Chen, and W. Cao, JOM **64**, 839 (2012).
[15] B. Cantor, I. T. H. Chang, P. Knight, and A. J. B. Vincent, Mater. Sci. Eng., A **375**, 213 (2004).
[16] B. Schuh, F. Mendez-Martin, B. Voelker, E. P. George, H. Clemens, R. Pippan, and A. Hohenwarter, Acta Mater. **96**, 258 (2015).
[17] E. J. Pickering, R. Munoz-Moreno, H. J. Stone, and N. G. Jones, Scr. Mater. **113**, 106 (2016).
[18] F. Otto, A. Dlouhy, K. G. Pradeep, M. Kubenova, D. Raabe, G. Eggeler, and E. P. George, Acta Mater. **112**, 40 (2016).
[19] A. Gali and E. P. George, Intermetallics **39**, 74 (2013).
[20] F. Otto, A. Dlouhy, C. Somsen, H. Bei, G. Eggeler, and E. P. George, Acta Mater. **61**, 5743 (2013).
[21] B. Gludovatz, A. Hohenwarter, D. Catoor, E. H. Chang, E. P. George, and R. O. Ritchie, Science **345**, 1153 (2014).
[22] M. H. Tsai, Entropy **15**, 5338 (2013).
[23] X. F. Wang, Y. Zhang, Y. Qiao, and G. L. Chen, Intermetallics **15**, 357 (2007).
[24] K. B. Zhang, Z. Y. Fu, J. Y. Zhang, J. Shi, W. M. Wang, H. Wang, Y. C. Wang, and Q. J. Zhang, J. Alloys Compd. **502**, 295 (2010).
[25] Y. F. Kao, S. K. Chen, T. J. Chen, P. C. Chu, J. W. Yeh, and S. J. Lin, J. Alloys Compd. **509**, 1607 (2011).
[26] S. Singh, N. Wanderka, K. Kiefer, K. Siemensmeyer, and J. Banhart, Ultramicroscopy **111**, 619 (2011).
[27] M. S. Lucas, L. Mauger, J. A. Munoz, Y. M. Xiao, A. O. Sheets, S. L. Semiatin, J. Horwath, and Z. Turgut, J. Appl. Phys. **109**, 07E307 (2011).
[28] K. B. Zhang and Z. Y. Fu, Intermetallics **28**, 34 (2012).
[29] S. G. Ma and Y. Zhang, Mater. Sci. Eng., A **532**, 480 (2012).
[30] L. Liu, J. B. Zhu, J. C. Li, and Q. Jiang, Adv. Eng. Mater. **14**, 919 (2012).
[31] Y. Zhang, T. Zuo, Y. Cheng, and P. K. Liaw, Sci. Rep. **3**, 1455 (2013).
[32] F. Tian, L. K. Varga, N. Chen, L. Delczeg, and L. Vitos, Phys. Rev. B **87**, 075144 (2013).
[33] M. K. Miller, J. M. Hyde, M. G. Hetherington, A. Cerezo, G. D. W. Smith, and C. M. Elliott, Acta Metall. Mater. **43**, 3385 (1995).
[34] S. S. Brenner, M. K. Miller, and W. A. Softa, Scr. Metall. **16**, 831 (1982).
[35] F. Zhu, H. Wendt, and P. Haasen, Scr. Metall. **16**, 1175 (1982).
[36] W. Ji, W. Wang, H. Wang, J. Zhang, Y. Wang, F. Zhang, and Z. Fu, Intermetallics **56**, 24 (2015).
[37] P. F. Yu, L. J. Zhang, H. Cheng, H. Zhang, M. Z. Ma, Y. C. Li, G. Li, P. K. Liaw, and R. P. Liu, Intermetallics **706**, 82 (2016).
[38] K. Jin, B. C. Sales, G. M. Stocks, G. D. Samolyuk, M. Daene, W. J. Weber, Y. Zhang, and H. Bei, Sci. Rep. **6**, 20159 (2016).
[39] D. Ma, B. Grabowski, F. Koermann, J. Neugebauer, and D. Raabe, Acta Mater. **100**, 90 (2015).
[40] F. Otto, N. L. Hanold, H. Bei, and E. P. George, Intermetallics **54**, 39 (2014).
[41] D. Kriegner, Z. Matej, R. Kuzel, and V. Holy, J. Appl. Crystallogr. **48**, 613 (2015).
[42] T. Zak and Y. Jiraskova, Surf. Interface Anal. **38**, 710 (2006).
[43] P. Hohenberg and W. Kohn, Phys. Rev. **136**, B864 (1964).
[44] W. Kohn and L. J. Sham, Phys. Rev. **140**, A1133 (1965).
[45] G. Kresse and J. Hafner, Phys. Rev. B **47**, 558 (1993).
[46] G. Kresse and J. Furthmüller, Phys. Rev. B **54**, 11169 (1996).
[47] P. E. Blochl, Phys. Rev. B **50**, 17953 (1994).
[48] G. Kresse and D. Joubert, Phys. Rev. B **59**, 1758 (1999).
[49] J. P. Perdew, K. Burke, and M. Ernzerhof, Phys. Rev. Lett. **77**, 3865 (1996).
[50] S.-H. Wei, L. G. Ferreira, J. E. Bernard, and A. Zunger, Phys. Rev. B **42**, 9622 (1990).
[51] U. Gonser, C. J. Meechan, A. H. Muir, and H. Wiedersich, J. Appl. Phys. **34**, 2373 (1963).

[52] W. Keune, R. Halbauer, U. Gonser, J. Lauer, and D. L. Williamson, J. Appl. Phys. **48**, 2976 (1977).
[53] J. Larrea J., D. R. Sánchez, F. J. Litterst, E. M. Baggio-Saitovitch, J. C. Fernandes, R. B. Guimarães, and M. A. Continentino, Phys. Rev. B **70**, 174452 (2004).
[54] I. S. Sandalov and A. N. Podmarko, Phys. Lett. A **109**, 76 (1985).
[55] C. Niu, A. J. Zaddach, A. A. Oni, X. Sang, J. W. Hurt III, J. M. LeBeau, C. C. Koch, and D. L. Irving, Appl. Phys. Lett. **106**, 161906 (2015).
[56] Y. Tsunoda, S. Imada, and N. Kunitomi, J. Phys. F **18**, 1405 (1988).
[57] A. Onodera, Y. Tsunoda, N. Kunitomi, O. A. Pringle, R. M. Nicklow, and R. M. Moon, Phys. Rev. B **50**, 3532 (1994).
[58] E. Vincent, in *Ageing and the Glass Transition,* edited by M. Henkel, M. Pleimling, and R. Sanctuary, Lecture Notes in Physics Vol. 716 (Springer, New York, 2007).
[59] P. Pal, A. K. Majumdar, and A. K. Nigam, J. Magn. Magn. Mater. **381**, 297 (2015).
[60] A. Cakir, M. Acet, and M. Farle, Sci. Rep. **6**, 28931 (2016).
[61] J. Nogues, J. Sort, V. Langlais, V. Skumryev, S. Surinach, J. S. Munoz, and M. D. Barob, Phys. Rep. **422**, 65 (2005).
[62] R. Rana, P. Pandey, R. P. Singh, and D. S. Rana, Sci. Rep. **4**, 4138 (2014).
[63] U. Meesala, S. P. Mathew, and S. N. Kaul, J. Alloys Compd. **685**, 122 (2016).
[64] J. S. Kouvel, J. Phys. Chem. Solids **24**, 795 (1963).
[65] K. Sato, H. Katayama-Yoshida, and P. H. Dederichs, Psi-k Newsl. **70**, 93 (2005).
[66] T. P. C. Klaver, R. Drautz, and M. W. Finnis, Phys. Rev. B **74**, 094435 (2006).
[67] R. E. W. Casselton and W. Hume-Rothery, J. Less Common Met. **7**, 212 (1964).
[68] J. S. Kasper and J. S. Kouvel, J. Phys. Chem. Solids **11**, 231 (1959).
[69] E. Kren, E. Nagy, I. Nagy, L. Pal, and P. Szabo, J. Phys. Chem. Solids **29**, 101 (1968).
[70] P. R. Garnier and M. B. Salamon, Phys. Rev. Lett. **27**, 1523 (1971).
[71] V. E. Panin and V. P. Fadin, in *Order-Disorder Transformations in Alloys*, edited by H. Warlimont (Springer-Verlag, Berlin, Heidelberg, 1974).
[72] K. Momma and F. Izumi, Commission on Crystallogr. Comput., IUCr Newslett. **7**, 106 (2006).
[73] K. Momma and F. Izumi, J. Appl. Crystallogr. **41**, 653 (2008).
[74] K. Momma and F. Izumi, J. Appl. Crystallogr. **44**, 1272 (2011).